

NASA Technical Memorandum 73251

(NASA-TM-73251) PRELIMINARY ANALYSIS OF
REMOTE INFRARED IMAGERY OF SHUTTLE DURING
ENTRY: AN AEROTHERMODYNAMIC FLIGHT
EXPERIMENT (NASA) 30 p HC A03/MF A01

N77-31449

Unclass

CSCL 20D G3/34 47444

Preliminary Analysis of Remote Infrared Imagery of Shuttle During Entry - An Aerothermodynamic Flight Experiment

Byron L. Swenson and Larry E. Edsinger

AUGUST 1977



NASA

NASA Technical Memorandum 73251

**Preliminary Analysis
of Remote Infrared Imagery
of Shuttle During Entry -
An Aerothermodynamic
Flight Experiment**

Byron L. Swenson and Larry E. Edsinger

Ames Research Center
Moffett Field, California



National Aeronautics
and Space Administration

**Scientific and Technical
Information Office**

1977

PRELIMINARY ANALYSIS OF REMOTE INFRARED IMAGERY OF SHUTTLE

DURING ENTRY — AN AEROTHERMODYNAMIC FLIGHT EXPERIMENT

Byron L. Swenson and Larry E. Edsinger

Ames Research Center

SUMMARY

The preliminary feasibility of remote high-resolution infrared imagery of the Shuttle Orbiter lower surface during entry to obtain accurate measurements of aerodynamic heat transfer to that vehicle has been examined. In general, it was determined that such images can be taken from an existing aircraft/telescope system (the C-141 AIRO) with a minimum modification or addition of systems using available technology. These images will have a spatial resolution of about 0.3 m and a temperature resolution much better than 2.5 percent. The data from these images will be at conditions and at a scale not reproducible in ground based facilities and should aid in the reduction of the prudent factors of safety required to account for phenomenological uncertainties on the thermal protection system design. Principal phenomena to be observed include laminar heating, boundary-layer transition, turbulent heating, surface catalysis, and flow separation and reattachment.

INTRODUCTION

In a few years, the Space Shuttle reusable space transportation system will begin regular and frequent operation to and from Earth orbit. Recently it has been recognized that this regular operation will present an unparalleled opportunity to obtain a variety of entry aerothermodynamic flight data. These data can be obtained at flight conditions and scale not reproducible in ground based facilities and are thus extremely important to the verification and refinement of existing computational and experimental extrapolation techniques. These refinements should allow a considerable reduction in the prudent factors of safety which are used to account for several phenomenological uncertainties associated with thermal protection system design. These data, therefore, can have a significant effect upon the design and performance of future systems.

One of the aerothermodynamic experiments suggested for Shuttle entry is the use of remote high-resolution infrared imagery of the lower and side surfaces of the Shuttle Orbiter to measure surface temperature and thus to infer aerodynamic heating. This inference is easily made due to the low diffusivity of the reusable surface insulation material used for thermal protection. The surface is, therefore, very nearly in radiation equilibrium

and the aerodynamic heating is proportional to the fourth power of surface temperature. There will be, of course, on-board thermocouple measurements of surface temperature, but these measurements are necessarily limited in number by many considerations and will only provide coarse resolution of surface temperature distribution. If remote imagery can be utilized at reasonably high resolution (say, at least 1 m) then, for the instant and flight conditions of the exposure, highly accurate temperature distributions over the entire windward side of the vehicle will be obtained. Several such exposures taken at different times in the entry trajectory when coupled with the coarse resolution thermocouple data will provide accurate surface temperature distributions over the entire windward surface and temporally over the entry trajectory. These data obtained under real flight conditions will allow a detailed examination of flow phenomena such as boundary-layer transition, flow separation and reattachment, surface catalysis, and flow/surface interactions.

The purpose of this report is to examine in a preliminary manner the technical feasibility of this experiment. This analysis will focus on attaining an understanding of the tradeoffs between measurement resolution and accuracy (signal-to-noise ratio) and the sensor and optics systems which are available. In addition, the image acquisition requirements and data handling problems will also be examined.

DISCUSSION

The discussion that follows will first describe the Shuttle Orbiter entry trajectory and expected heating environment. From that description, the experimental requirements will be established in terms of resolution and temperature measurement level and accuracy and the most desirable Shuttle flight conditions for the images. Next, the existing imaging systems that might be appropriate for this experiment will be described. Then the highly interactive technical aspects of image acquisition, acquisition system design and response, primary sensor type and response, primary optics and plate scale, and data handling will be examined.

Shuttle Entry Trajectory and Environment

The Shuttle Orbiter vehicle is shown in two views (bottom and side) in figure 1. The length of the body is approximately 32 m. Some of the details of a typical entry trajectory of the orbiter are shown in figure 2. The top two figures indicate a typical time history of velocity and altitude. The bottom two figures indicate a corresponding time history of angle of attack, α , and angle of bank, β , as the orbiter ranges toward the landing site. Typically, entry is initiated at a high angle of attack (approximately 40°) and at zero bank until the vehicle pulls out into equilibrium glide at an altitude of about 74 km. The angle of attack is then decreased and the vehicle is pitch and roll modulated as it descends and ranges to the landing site.

The peak radiation-equilibrium temperatures expected during entry are indicated by the isothermal contours shown in figure 1. Peak temperatures near the nose of the vehicle occur near the time of pullout or about 450 sec into the entry trajectory and are about 1700 K. Peak temperatures farther aft on the vehicle occur at later times in the trajectory at about 800 to 1100 sec after entry and are in the range of 1200 K. Peak temperatures on the side of the vehicle range from 700 to 900 K. After about 1300 sec the most severe part of the entry heating pulse is over.

The contours shown in figure 1 are peak temperature isotherms and do not indicate the true range of temperatures to be expected over the surface at a given instant in time. This range is indicated more completely in figure 3 where the lower centerline temperature distribution is shown for two times during entry. Temperatures as low as about 900 K are observed. The temperature distribution shown for an entry time of 450 sec is the result of completely laminar flow. The substantial increase in temperature over the aft 20 percent of the vehicle at 1100 sec is caused by boundary-layer transition to turbulent flow.

The transition of boundary-layer flow from laminar to turbulent is, of course, one of the phenomena of greatest experimental interest. Figure 4 shows the expected location and movement of the start and end of transition during entry. It can be seen that transition begins about 800 sec after entry at the vehicle trailing edge and starts to move forward. It is also apparent that the transition region at any time extends over about 10 to 20 percent of the vehicle length or about 3 to 6 m.

Another important aspect of the entry environment is the effect of control deflection on flow separation and control heating. During the early part of the entry trajectory the vehicle is trimmed to a high angle of attack with the body flap retracted from the flow. At pullout (about 450 sec) the body flap is deflected into the flow to trim the vehicle to a lower angle of attack. Flow separation is expected to develop in front of the flap with reattachment on the flap and a corresponding high heating rate and equilibrium temperature. The temperature distributions over the body-flap juncture are shown in figure 5 for 450 and 800 sec after entry. Temperatures in this region range from 700 to 1700 K. The separated flow region is about 3 percent of the body length or about 1 m.

Experiment Requirements

Based on the foregoing discussion, there are at least four times during a typical entry trajectory when it would be desirable to have high-resolution infrared images of the Shuttle Orbiter. These times are: (1) at about 450 sec after entry when the laminar heating peaks on the vehicle; (2) at about 800 sec after entry when significant control deflections are being made and the flap heating is maximum; (3) at about 1100 sec after entry when boundary-layer transition has occurred near the trailing edge of the vehicle and some fully developed turbulent flow is present; and (4) at about 1300 sec when the lower surface is dominated by turbulent boundary-layer flow.

Table 1 indicates the velocity, altitude, and attitude of the vehicle at those times.

The temperature range of the images for each of these entry times is indicated in table 2. The surface resolution requirements for these temperatures depend, of course, upon the size of the phenomena to be observed. At 450 sec, when the aerodynamic heating is laminar, a resolution of 1 m (3 percent of vehicle length) will provide an excellent view of the heating distribution. For the 800 sec flight condition, details of the flow over the flap are desired and a resolution of about 0.3 m would be required to adequately image the separated flow region. For images taken at 1100 to 1300 sec after entry where detail of boundary-layer transition is desired, a resolution of 1 m will provide adequate information over the 3 to 6 m transition front.

In addition to images of the lower surface at four times during entry, examination of figure 2(d) shows that the vehicle is rolled (banked) at these times to angles between 40° and 80°. This allows images to be taken either of the lower surface (windward surface) or of side surface by an appropriately positioned imaging system located on one or the other side of the Shuttle Orbiter ground track. A resolution of 0.3 m or about 6 percent of the height of the vehicle body will provide adequate detail on the aerodynamic heating to the side surface.

The accuracy of temperature measure for all cases should, in general, result in a measurement of aerodynamic heating rate superior to that obtained in wind tunnels. In general, the accuracy of wind-tunnel heat transfer measurements is about 10 to 20 percent. Since the measured surface temperature varies as aerodynamic heating rate to the one-fourth power, a temperature measurement accuracy of 2.5 percent should be a design goal for the infrared imaging experiment.

In summary then, the measurement design requirements for this experiment are the following:

1. At least four times during the entry trajectory are of principal interest, that is, at 450, 800, 1100, and 1300 sec after entry on the nominal entry trajectory.
2. Excellent data will be obtained at a resolution of 1 m. However, the details of flow separation induced by the body flap and details of the heating to the side surface would require a resolution of 0.3 m.
3. The dynamic range requirements of images taken at the times of principal interest are indicated in table 2.
4. The accuracy of the temperature measurements contained in the thermal images should be 2.5 percent.

Imaging Systems

At this writing there are at least five existing optical facilities which might be used for this experiment; four are airborne and one is ground based:

1. The C-141 Airborne Infrared Observatory (AIRO) operated by NASA at Ames Research Center with a 91.5 cm Cassegrain telescope.
2. The NASA-Ames Research Center Learjet with a 30-cm telescope.
3. The NASA-Ames Research Center CV-990 with a 30-cm Cassegrain telescope.
4. The KC-135 Terminal Radiation Project aircraft (TRAP 7) operated by the USAF with a 15 cm telescope.
5. The ARPA Maui Optical Station (AMOS) located at the crest of Mount Haleakala on Maui, Hawaii. This facility has two 122 cm and one 160-cm Cassegrain telescopes. This facility is only of interest, of course, if an appropriate part of the Shuttle entry trajectory is observable from this fixed location. The first four Shuttle flights are currently planned to be recovered at the Dryden Flight Research Center in California and the early part of the entry may be visible from Hawaii.

All of these telescopes are designed for diffraction-limited operation at a wavelength of about $1 \mu\text{m}$. The angular resolution of diffraction-limited telescopes for a wavelength of $1 \mu\text{m}$ as a function of aperture diameter is shown in figure 6. The resolution criteria used is the Rayleigh criterion. As indicated on the figure, diffraction-limited operation is further limited by atmospheric turbulence and for airborne systems by the turbulence in the air flow near the body of the aircraft. Experience indicates that this limit from airborne system is about 10 $\mu\text{radians}$ for open-port telescopes, and it is expected that this limit can be reduced to about 5 $\mu\text{radians}$ (1 arc sec) with the use of an optical window. It is apparent that the angular resolution of all telescope options, with the exception of the smaller 15 cm optics on-board the TRAP-7 aircraft, will provide an angular resolution of about 5 $\mu\text{radians}$. A resolution of 10 $\mu\text{radians}$ is realized for the 15-cm optics.

Each of the existing imaging systems considered has its advantages and disadvantages. Each system will require some modification. For the purposes of ascertaining the technical feasibility and tradeoffs associated with this experiment, only one system, the C-141 AIRO, will be considered further in this report.

The telescope on the C-141 AIRO is mounted ahead of the wing and looks out athwartship on the left-hand side of the aircraft as shown in figure 7. It is movable in elevation from 35° to 75° above the horizon. The maximum slew rate for the telescope is $0.08^\circ/\text{sec}$. The telescope can also be vignetted 2° forward and aft. The telescope is a Cassegrain design with

normal focus f number of f/10 or with a bent-focus at f/13.5. The field of view for these two focal configurations is 20 and 14 arc min, respectively. A complete description of the aircraft-telescope system is contained in reference 1. The nominal aircraft operating conditions are about 14 km altitude and 0.2 km/sec.

Image Acquisition

There are basically two modes of image acquisition possible with the AIRO. The first mode involves target acquisition by a wide-field acquisition system, directing the main telescope to the target, and tracking the target (slewing the telescope) as the Shuttle flies by overhead. The only reason to slew the telescope is to increase the exposure time by providing image motion compensation. This target-tracking mode requires slewing in elevation angle; thus, the AIRO must be flying a path crossing the Shuttle ground track downrange of the Shuttle and crossing from right to left. The geometry of this encounter is shown schematically in horizontal and vertical views in figure 8 for imagery of the 450 sec-after-entry flight condition. As can be seen, for this case, the Shuttle Orbiter comes into the elevation range of the telescope at a range of about 106 km and is in view for 9.4 sec. The tracking or slew rates are quite high; starting at $2.3^\circ/\text{sec}$ and building up to $6.7^\circ/\text{sec}$ over the encounter. In order not to require a vignette of the telescope, the aircraft should cross the Shuttle ground track at an angle of 88.5° .

The tracking rates for this mode are quite high, much higher than the current AIRO capability, but the main difficulty with the tracking mode is the disastrous effects of Shuttle ground track and altitude uncertainties. The position uncertainties of the Shuttle Orbiter are caused by execution errors on the deorbit maneuver and atmosphere density uncertainties at high altitude. At a given instant in the entry trajectory the Shuttle will be found with high probability in an ellipsoid in space about 15-km wide in the crossrange direction, possibly 20-km long in the downrange direction, and about 3 km in altitude variation. Both the crossrange and downrange errors would either require a substantial fore or aft vignette of the telescope, much larger than the telescope mount capability, or a coordinated turn by the aircraft. The coordinated turn would require that the aircraft autopilot obtain inputs from the wide-field acquisition telescope. This mode is relatively insensitive to altitude uncertainties.

The second image acquisition mode involves target acquisition by a wide field acquisition system, tracking the target and predicting its path, directing the telescope field of view to that path, and acquiring images as the target passes through the field of view. This mode is limited to very short exposure times; short enough to eliminate image smear. This mode might be termed "path acquisition" as opposed to "target acquisition" for the previous mode. The most advantageous geometry for the encounter is shown schematically in horizontal and vertical views in figure 9 again for the 450 sec after entry flight condition. In this case the aircraft flies a parallel offset flight path to the right side of the Shuttle ground track.

The Shuttle overtakes the aircraft and flies through the field of view of the main telescope. The range at that time is the range of closest approach and is a function of the flight path offset and the associated elevation angle to the target. At an elevation angle of 60° the range is nominally 70 km. For this mode, acquisition of the Shuttle is accomplished to the aft of the aircraft. The main telescope is steered to the proper elevation angle such that the Shuttle flight path passes through the field of view. Crossrange and altitude uncertainties are reflected by steering in elevation angle from a nominal expected elevation angle. This mode is completely insensitive to downrange errors as this error effects only the time of the image (less than ± 1.5 sec).

If the Shuttle is banked for a left turn then the image obtained by this mode as illustrated in figure 9 is that of the lower surface. If the Shuttle is banked for a right turn then the image is that of the right side surface. Of course, if images of the lower surface are desired for the right-turn bank condition then the aircraft must fly a parallel flight path to the left of the Shuttle ground track and heading toward the oncoming Shuttle. The small change in relative velocity will have no effect, but acquisition must be accomplished forward of the aircraft. Thus, the acquisition system must be flexible enough to accommodate both forward and aft viewing angles.

To reiterate, considering all aspects of the problem of image acquisition, it appears that the second mode, "path acquisition," is the most desirable. The major drawback for this mode is the requirement for extremely short exposure times. For the expected angular resolution of 5 μ rad, for a range of 70 km, and for a target relative velocity of 7.3 km/sec, the Shuttle will move one resolution element in about 48 μ sec. The resolution of the images at a nominal range of 70 km is about 0.35 m.

Acquisition System

The field of view of the acquisition system must be large enough to more than encompass the positional uncertainties of the Shuttle. For the "path acquisition" mode the system must also be capable of either looking aft or forward at a sufficiently large angle to provide enough time to acquire the target, predict its path, and correct the elevation angle of the main telescope. The operation of the acquisition system is shown diagrammatically in figure 10. The Shuttle is centered in the acquisition system field of view and tracked toward closest approach. The elevation and azimuth angles are picked off of the acquisition telescope which are then fed to the computer to predict the Shuttle flight path producing an error signal which is used to correct the elevation angle of the main telescope. It appears that a line-scanning system utilizing an appropriate linear array of photoconductors could be used for the acquisition sensor. The field of view of the acquisition telescope could be scanned over the fixed linear array by a rotating many-sided mirror drum.

The field of view of the main telescope of the AIRO is 20 arc min for the normal focus or 14 arc min for the bent-focus. At closest approach (70 km) the Shuttle length subtends about 0.4 mradian or about 1.4 arc min. In order

to assure that the Shuttle will be in the field of view at closest approach the acquisition system should be able to predict the position of the Shuttle in elevation angle to an accuracy of perhaps 5 arc min. This would require an angular resolution or pixel size of the acquisition system to be somewhat smaller than 5 arc min; perhaps as small as 1.4 arc min.

The positional uncertainties of the Shuttle at the acquisition range (say, 100 km) dictates minimum size of the field of view to be scanned. For the positional uncertainty ellipsoid previously quoted, the field of view should be about 10° . This field of view together with the pixel size requirement translates into a requirement for a linear array about 400 elements long which is well within the current state of the art. Using an element size of 0.1 mm produces an image frame size of 4 cm^2 . The focal length of the system for a 10° field of view is 22.9 cm.

The scan rate of the acquisition system is determined by details of the tracking loop, servo mechanisms, and computer filtering of the tracking data which are beyond the scope of this paper. Suffice it to say that the scan rate must be fast enough to assure that a prediction of the Shuttle flight path can be obtained to an elevation angle accuracy of 5 arc min with sufficient lead time to allow for the elevation correction of the main telescope. In order to facilitate the following calculation of the acquisition signal-to-noise ratio, a scan rate of 30 acquisition frames/sec was assumed. The tracking time available from a 100-km acquisition range to closest approach is about 9 sec (fig. 9). Sampling at 30 frames/sec will supply the computer with over 200 data points to make its projection. The assumed framing rate for a 400×400 element frame results in detector dwell time of each sensor element of 83 μsec .

Since the Shuttle image in the acquisition system is always unresolved, that is, smaller than a single pixel, the power received by that pixel is given by the following expression

$$I = \int_s \int_{\lambda_1}^{\lambda_2} \frac{W_\lambda}{\pi} d\lambda ds \left[\epsilon T_a T_o \left(\frac{\pi D^2}{4 R^2} \right) \right] \quad (1)$$

where the double integral represents the blackbody radiation per steradian obtained by integrating the spectral emittance, W_λ , over the wavelength regime of the bandpass filter and over the body surface, s . The other factors are ϵ , the surface emissivity (taken as 0.85); the transmission of the atmosphere and optical system including the bandpass filter, T_a and T_o (taken conservatively as 0.98 and 0.5), respectively; the aperture diameter of the acquisition optics, D ; and the range to the target, R .

The signal-to-noise ratio for a solid state sensor can then be obtained by comparing the signal I , with noise equivalent power (NEP) for several candidate sensor materials. The noise equivalent power (see ref. 2) is expressed by

$$NEP = \frac{(A\Delta f)^{1/2}}{D^*} \quad (2)$$

where A is the area of the sensor element, Δf is the noise equivalent bandwidth, and D^* is the specific detectivity of the sensor material. The noise equivalent bandwidth, Δf , is related to the detector dwell time, t , by

$$\Delta f = \frac{\pi}{4t} \quad (3)$$

Utilizing these relationships and the spectral response (D^*) for several state-of-the-art materials, the acquisition signal-to-noise ratios for two of the Shuttle flight conditions of interest, for a 100 km acquisition range, and for an example, 5-cm f/4.6 acquisition system aperture are given in table 3. Because of the high assumed framing rate (30/sec) and the corresponding low detector dwell time (83 μ sec) the sensor material candidates are limited to low-time-constant materials. These candidates are lead selenide (PbSe), indium arsenide (InAs), and indium antimonide (InSb). The appropriate bandpass filter for these materials is 1.4 to 1.9 μ m to coincide with an atmospheric window.

The specific detectivity for these materials at the operating temperatures indicated were obtained from commercial sources (e.g., private communication from Santa Barbara Research Center Marketing Dept., Goleta, California). It can be seen that there is a more than adequate signal-to-noise ratio for detection in all cases except for the use of lead selenide (PbSe) at ambient operating temperatures (295 K). All these sensors have a linear response up to signal-to-noise ratios of at least 10^4 . The bandpass filter can be modified to reduce the signal to the linear dynamic range, if required. Using any of these materials for the acquisition sensor requires some detector cooling.

The use of any of the above photoconductor or photovoltaic materials also requires a line-scan system in order to keep the noise equivalent bandwidth below 10 kHz at a framing rate of 30/sec. It is also possible to use an extremely fast sensor material like mercury cadmium telluride (HgCdTe) in a spot scanning system mode where a single detector element is scanned across a line and then is rastered in an orthogonal direction to scan the scene. The cycle time per picture element for a 400 \times 400 pixel frame at 30 frames/sec is about 0.2 μ sec or the noise equivalent bandwidth is about 3.8 MHz. A HgCdTe sensor has maximum sensitivity to infrared wavelengths near 10 μ m. For this reason a bandpass filter of 9.5 to 10.5 μ m would be used with such system to coincide with an atmospheric window. Of course, if an optical window is required for the acquisition system, then transmission at these wavelengths dictates the necessity of a barium fluoride window.

Utilizing the relationships above, the acquisition signal-to-noise ratios at a range of 100 km for a HgCdTe spot scanning system and for the 450 and 1100 sec image conditions are indicated in the last column in table 3.

The resulting signal-to-noise ratios for the spot scanning system are completely inadequate for two reasons. The signal near a wavelength of $10\text{ }\mu\text{m}$ is quite a bit lower than near $2\text{ }\mu\text{m}$ and the relatively high frequency operation of the sensor results in a much higher noise equivalent power.

In summary then, it appears from this preliminary examination of the acquisition system design that a line scan system appears feasible using about 400 elements in a linear array and scanning at 30 frames/sec. At least three photoconductor or photovoltaic sensor materials provide more than adequate signal-to-noise ratio for acquisition at ranges up to 100 km. A small telescope aperture with a diameter of 5 cm and a focal length of 22.9 cm appears adequate for the acquisition systems.

Primary Imaging System

The primary imaging system will utilize the 91.5-cm optics contained on-board the AIRO as described in reference 1. As discussed before, the "path acquisition" mode produces a requirement for very fast exposures to minimize the effects of image smear. With no image motion compensation, the image will move the distance of one resolution element in $48\text{ }\mu\text{sec}$. The choice of primary sensor is thus dominated by the requirement for very fast response.

There are several current state-of-the-art candidates for the primary sensor. These candidates are high-speed infrared photographic film, photoconductive or photovoltaic sensors in the form of linear arrays of sensitive elements, and back illuminated silicon charge coupled devices (CCD) in the form of area arrays of sensitive elements. The main disadvantage of film is that its sensitivity falls off sharply at about $0.9\text{ }\mu\text{m}$. For the surface temperatures of interest in this experiment, there is insufficient signal at the shorter wavelengths for exposures of the order of microseconds. In addition, film does not possess enough dynamic range for this application and thus will not be considered further.

Linear arrays—Semiconductor linear arrays can be used in two ways in this application to produce the desired image. First, the linear array can be fixed vertically across the image plane and the Shuttle Orbiter will be scanned by its own horizontal motion across the field of view. This mode might be termed a "streak camera" mode. Multiple images can be obtained during the encounter by arranging a number of linear arrays across the image plane such that the image of the Shuttle Orbiter encounters each linear array sequentially as shown schematically in figure 11. Each of such images will be identical since the heat transfer conditions to the Shuttle will not change during the 40 msec that the Shuttle is in the field of view. These multiple images will be valuable for the purposes of computer enhancement.

The second method of obtaining images with a linear array is to scan the scene with the array using it in a "pushbroom" fashion. Multiple images would be obtained by multiple scans of the field of view during the

40 msec imaging period. Scanning would only be attractive, however, if the scan is performed in the direction of motion of the Shuttle image in order to provide some image motion compensation. However, it will be shown that the sensor response is sufficiently fast and that the signal-to-noise ratio is sufficiently high in the streak camera mode to eliminate the necessity of image motion compensation.

In order to obtain the proper sensor response, the time constant of the sensor material should be much smaller than the available exposure time. In order to achieve a 99 percent response to a given signal change, an exposure time of about 5 time constants is required. Thus, if 48 μ sec are available for the scan of one resolution element, then the material time constant should be about 9 μ sec or less. There are at least ten such material candidates with this fast response capability. The characteristics of these materials are listed in table 4. The last four candidates can be rejected because of the complication involved with helium cryogenic cooling and because the peak response for these sensors is at very long wavelengths. The third through the sixth candidates are also rejected because their peak response is at longer wavelengths. The three remaining candidates are all viable alternates. Indium antimonide (InSb) is chosen over gold-doped germanium (Ge:Au) because, although its peak response is at 5 μ m, the specific detectivity, D^* , of InSb is considerably higher than Ge:Au at 1 to 2 μ m.

Whichever sensor is chosen, the size and spacing of the sensor elements should be matched in the focal plane to the plate scale and angular resolution capability of the telescope, and in a manner which minimizes the "cross-talk" between sensor elements caused by diffractive spreading of the signal. As noted above, the existing AIRO telescope can be operated in two configurations, one giving a 20 arc min field of view with 53.2-mm focal plane and another giving a 14 arc min field of view with a 50.3-mm focal plane.

The resolution of the telescope is limited to an angular resolution of 5 μ radians by the turbulence in the air flow past the telescope port window. Dividing the field of view by the 5 μ radians resolution produces a requirement for about 1100 and 800 elements to span the 20 and 14 arc min fields of view, respectively. A larger number of sensors will not improve resolution and would increase data handling requirements. The spacing of these elements is about 0.05 mm in the focal plane.

For the candidate sensors, the smallest commercially available sensors are about 0.10 mm². Thus, the required 0.05 mm element spacing creates a problem. There are two approaches to the solution of this problem. First, auxiliary optics can be used to increase the physical size of the focal plane by about a factor of two. Then the sensor elements would match the size of the resolution elements and the element could be arranged in a single column. Second, if the signal is sufficiently strong the elements could be staggered in focal plane as shown schematically in figure 12. The detectors could then be masked to a small size (diameter, d) sufficient to eliminate overlap. Because of its simplicity this second approach will be examined to determine the required size of the hole diameter in the masking.

The size of the opening in the mask over the sensor elements is dictated by the signal and the desire to minimize element to element "cross-talk." This cross-talk is a result of the superposition of the diffraction patterns from adjacent resolution elements on an individual element. It would be desirable to size the sensor elements such that only part of the central maximum of the diffraction pattern is used for sensing thereby minimizing the amount of the diffraction pattern from adjacent points that are also detected. However, this can only be done if the signal is sufficiently strong.

The total signal from a resolved surface element on the Shuttle Orbiter focused in the image plane is given by the following expression

$$I = C(d) \int_{\lambda_1}^{\lambda_2} \frac{W_\lambda}{\pi} d\lambda \left(\frac{\pi}{4}\right) (\Delta\omega R)^2 \left[\epsilon_a^T \epsilon_o^T \left(\frac{\pi D^2}{4R^2}\right) \right] \quad (4)$$

where the integral represents the blackbody radiation per steradian obtained by integrating the spectral emittance, W_λ , over the wavelength regime of the bandpass filter. The angular resolution, $\Delta\omega$, is taken as 5 μ radians. The other parameters are as defined in equation (1) for the acquisition system except for D , the aperture is taken as 91.5 cm. Note that for a resolved image the signal is independent of range, R . Of course, all the signal, I , is not focused on an individual sensor element but is spread out in the full diffraction pattern. The constant, C , represents the fraction of total power received by the sensor element and is a function of mask hole diameter, d . The constant C is shown as function of the mask hole diameter in figure 13.

The signal-to-noise ratio for a resolved surface element can be obtained by comparing the results given by equation (4) with the noise equivalent power, NEP , given by equations (2) and (3). The area, A , in equation (2) in this case is the total size of the unmasked detector element (i.e., 0.1×0.1 mm). The noise equivalent bandwidth, Δf , is given by equation (3), where the detector dwell time is about 48 μ sec per resolution element. The signal-to-noise ratio for a sensor mask hole diameter of 0.04 mm is shown as a function of surface temperature for the range of interest (600 to 1400 K) in figure 14. The specific detectivities, D^* , for the three candidate sensor materials were obtained from commercial sources (Santa Barbara Research Center Marketing Dept.). It can be seen there is adequate signal-to-noise ratio for InSb and InAs sensors except for surface temperatures in the range of 600 to 700 K. PbSe sensors are not sufficiently sensitive to detect temperature below about 1000 K. For these candidate sensors, the high signal-to-noise ratios for high surface temperatures are not a problem in that the sensors do not saturate and have a linear response up to signal-to-noise ratios of at least 10^4 . The only way to obtain an acceptable signal for the low surface temperatures is to provide image motion compensation. For example, the sensor dwell time would have to be increased by a factor of 4 to double the signal-to-noise ratio.

For a resolved image, the total signal received is less important than the detectable contrast in the image; the contrast being given in terms of the minimum detectable temperature differential. The minimum detectable temperature differential, ΔT , is ideally that temperature differential which will produce a signal differential equal to the detector noise. Therefore,

$$\left. \begin{array}{l} \frac{dI}{dT} \Delta T = NEP \\ \text{or} \\ \Delta T = \frac{NEP}{dI/dT} \end{array} \right\} \quad (5)$$

Utilizing equations (2), (3), (4), and (5) and the spectral response (D^*) for the three candidate sensor materials, the minimum detectable temperature differential, ΔT , has also been calculated for the range of surface temperature of interest. The results of these calculations are shown in figure 15 again for a sensor mask hole diameter of 0.04 mm. Also indicated on the figure is the experiment design goal of a temperature measurement error less than 2-1/2 percent. It can be seen that for InSb and InAs sensors this goal is easily realized except for surface temperatures in the range of 600 to 700 K. Again PbSe sensors are not sufficiently sensitive to meet the design goal except at the highest temperatures.

Area arrays— Recently, back-illuminated silicon charge-coupled devices (CCD) in the form on an area array have reached a high state of development. Area arrays of 400×400 elements are commercially available. Work on arrays of up to 800×800 elements is underway. These sensor arrays are very sensitive to visible light in the orange and red end of the spectrum and to wavelengths in the near infrared out to about 1 μm . The relative response of these sensors to wavelength is shown in figure 16. The noise level for these devices is given in terms of a noise equivalent exposure which is 2×10^{-10} Wsec/cm². The physical size of the array is 9.2 mm² and each image element is 23 μm^2 . These sensors are fully described in reference 3.

The physical size of a CCD array is too small for the focal plane of the AIRO telescope. Auxiliary optics must be employed to decrease the physical size of the focal plane by about a factor of 2. Then four 400×400 element CCD arrays can be used to fill the field of view with each sensitive element matched in size to the limit resolution of the telescope.

Again the total received signal from a resolved surface element is given by equation (4). However, since CCD arrays have a variable response to light of different wavelengths in the range of 0.4 to 1.0 μm , equation (4) must be modified to include this relative response. This is done by multiplying the spectral emission, W_λ , by the relative response and then integrating over the wavelength regime. The signal-to-noise ratios of the measurements are obtained by comparing the received energy per unit area of the sensitive element over the exposure time with the noise equivalent exposure (2×10^{-10} Wsec/cm²). Thus the signal-to-noise ratio is

$$\frac{S}{N} = \frac{It_e/A}{2 \times 10^{-10}} \quad (6)$$

where A is the area of a sensitive element ($23 \times 23 \mu\text{m}$) and t_e is the exposure time. To limit smear it would be desirable to limit the exposure to less than $24 \mu\text{sec}$ (one-half resolution element smear). The calculated S/N as a function of temperature is shown in figure 17 for an exposure time of $10 \mu\text{sec}$. It can be seen that an inadequate signal-to-noise ratio exists for surface temperatures less than 700 to 800 K. In addition, CCD arrays become saturated at a S/N of about 5000 thus limiting radiometric measurements to temperatures less than about 1100 K. This saturation limit can be extended to higher temperatures at the expense of S/N at lower temperatures by reducing the exposure time or by decreasing the bandpass of the observation.

The minimum detectable temperature differential as a function of surface temperature for the CCD array has also been calculated and is displayed in figure 18. It can be seen that a 2-1/2 percent accuracy can be realized for temperatures greater than about 700 K.

Summary— After examining the merits of several types of primary sensors, it appears that the best engineering solution is to use a linear array of 800-1000 photoconductive or photovoltaic indium antimonide or indium arsenide sensors in a "streak camera" mode. Adequate signal exists for highly accurate measurements (errors less than 2-1/2 percent) of surface temperatures above 700 K. These detectors require cooling to 77 K and each sensor may require masking to a 0.04-mm-diameter circular sensitive area to match the plate scale on the AIRO telescope.

Data Handling

The total amount of data contained in an image of lower surface of the Shuttle Orbiter at the best resolution really is modest. If the data are digitized to 8 bits (sufficient accuracy for the temperature range of interest), then the total data in an image of the lower surface is less than 30,000 bits at a resolution of 0.3 m and if the background can be eliminated. The engineering problem associated with the data handling for this experiment is not with the amount of data but with the rapidity at which it must be taken.

With 800 detectors in the linear array to be sampled and read within $24 \mu\text{sec}$, the resulting sampling rate is 33 MHz. This rate is far beyond the capability of airborne instrumentation or even video recorders, which are limited to about 6 MHz analog data bandwidth. The first step in reducing the data rate is to read only those detectors which actually see the Shuttle. This can be done by placing trigger detectors in the focal plane ahead of the primary arrays. Each trigger detector would be associated with a small block of the primary array detectors; say, about 8. Thus, about 100 trigger detectors are required. At the limiting resolution of $5 \mu\text{rad}$,

the Shuttle image encompasses between 60 to 110 pixels in elevation depending on the time in the trajectory being observed. If, allowing some margin at the edges of the image, 16 blocks of 8 detectors each (128 detectors) are scanned in 24 μ sec, the sampling rate is reduced to about 5.3 MHz. This is still too high for relatively standard tape recorders.

The next step in reducing the read rate is to employ a buffer mechanism to reduce these rates to acceptable values. Analog shift registers (ASR) could be used as such a buffer. ASR's have typical capacities to delay and hold about 128 analog measurements. These measurements can be delayed for up to about 40 msec without any degradation. These devices can accept data at rates up to 12 MHz. By multiplexing the data stream from the 128 detectors into a series of these ASR's on a scan-by-scan basis, the resulting read rate can be reduced by increasing the number of ASR's. A block diagram of this data handling concept is shown in figure 19. If 4 ASR's are used, then the first ASR can be read during the time required for the next three scans so that it will be available for the fifth scan. The read rate is thus reduced by a factor of 3 to about 1.8 MHz. Of course, each of the 4 ASR's must be read in parallel into 4 separate tape recording tracks as indicated in figure 19.

Another alternative is to digitally buffer the data before recording. Since 128 pixels must be output in 24 μ sec, only 187 nsec are available to convert, switch, and store each pixel. A very high speed 8 bit analog-to-digital converter (ADC) has been developed by TRW (ADC-4) which can convert 13×10^6 samples/sec, or 77 nsec/pixel. The data must be loaded into a buffer in the remaining time. The Intel in-50 random access memory (RAM) can accept 10 parallel inputs from the ADC with an access time of 100 nsec. Other manufacturers produce RAM's with access times as short as 20 nsec. Therefore, this approach also appears feasible.

CONCLUSIONS

The preliminary feasibility of remote high-resolution infrared imagery of the Shuttle Orbiter lower surface during entry to obtain accurate measurements of aerodynamic heat transfer to that vehicle has been examined. In summary, the experiment appears, within the depth of the current analysis, both feasible and attractive. The most important technical conclusions are presented below.

1. There are at least four times during a typical entry trajectory when it would be desirable to have high-resolution infrared images of the Shuttle Orbiter. These times are (1) when laminar heating peaks on the vehicle, (2) when significant control deflections are being made and the flap heating is maximum, (3) when boundary-layer transition starts near the trailing edge of the vehicle, and (4) when the lower surface is dominated by a turbulent boundary layer.

2. A temperature range for the images of from 600 to 1700 K is expected, and an accuracy of at least 2.5 percent is desired.

3. The scale of the phenomena to be observed dictates a resolution requirement of at least 1 m.

4. The use of the C-141 Airborne Infrared Observatory with its 91.5-cm Cassegrain telescope to obtain such images is definitely feasible with a minimum modification or addition of systems. A small aperture (5-cm) acquisition system must be developed using indium antimonide detectors with appropriate servo mechanisms to command and drive the primary telescope. A focal plane system using 800 indium antimonide elements in a linear array is also required. Finally, a data handling system built of state-of-the-art components is required to handle the image plane data.

5. All elements of this experiment appear to be entirely feasible and employ only available technology.

Ames Research Center

National Aeronautics and Space Administration

Moffett Field, Calif., 94035, April 5, 1977

REFERENCES

1. NASA C-141 Airborne Infrared Observatory-Investigators Handbook, NASA Ames Research Center, Moffett Field, Calif.
2. Lloyd, J. M.: State-of-the-Art for Thermal Imaging. Optical Engineering, vol. 14, no. 1, Jan.-Feb. 1975, pp. 50-56.
3. Reilly, Terrence H.; and Herring, Mack: CCD Imaging Instruments for Planetary Spacecraft Application. Proc. of Symposium on Charge Coupled Device Technology for Scientific Imaging Applications, JPL Rep. SP 4321, June 15, 1975, pp. 46-64.

TABLE 1.- SHUTTLE ORBITER TRAJECTORY

Time from entry, sec	Velocity, km/sec	Altitude, km	Angle of attack, deg
450	7.53	74.4	41.5
800	5.73	63.7	32.8
1100	3.87	53.9	31.3
1300	2.29	44.2	28.5

TABLE 2.- IMAGE TEMPERATURE RANGES

Time from entry, sec	Temperature range, K
450	1700-1000
800	1700-700
1100	1700-600
1300	800-600

TABLE 3.- ACQUISITION SIGNAL-TO-NOISE RATIO FOR CANDIDATE DETECTORS AT GIVEN OPERATION TEMPERATURE

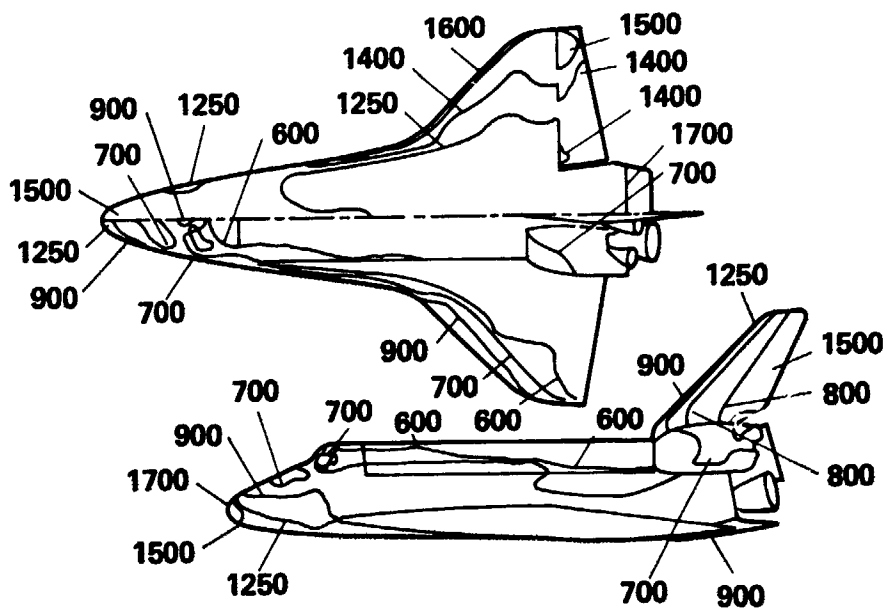
Time from entry, sec	Signal-to-noise ratio				
	PbSe	PbSe	InAs	InSb	HgCdTe
	295 K	193 K	77 K	77 K	77 K
	(a)	(a)	(a)	(a)	(b)
450	192	10300	261400	107500	2.8
1100	6.4	340	8640	3550	2.2

^a 5-cm aperture
 100-km range
 83- μ sec sensor dwell time (9.5 kHz)
 0.1-mm² elements - line scan system
 1.4 to 1.9- μ m bandpass filter

^b 0.2- μ sec sensor dwell time (3.8 MHz)
 0.1-mm² element - spot scan system
 9.5 to 10.5- μ m bandpass filter

TABLE 4.- LINEAR ARRAY SENSORS

Material	Operating temperature, K	Time constant, μ sec	Peak response, μ m
PbSe	295	3	3.8
InAs	77	5	3.0
InSb	77	.2	5.0
PbSnTe	77	2	10.0
HgCdTe	77	.8	10.6
Ge: Au	77	.1	5.0
Ge: Hg	4	.1	10.4
Ge: Cu	4	.1	21.0
Ge: Cd	4	.1	19.0
Ge: Zn	4	.1	37.0



NOTE: ALL TEMPERATURES IN K

Figure 1.- Shuttle orbiter plan and side views with maximum temperature contours.

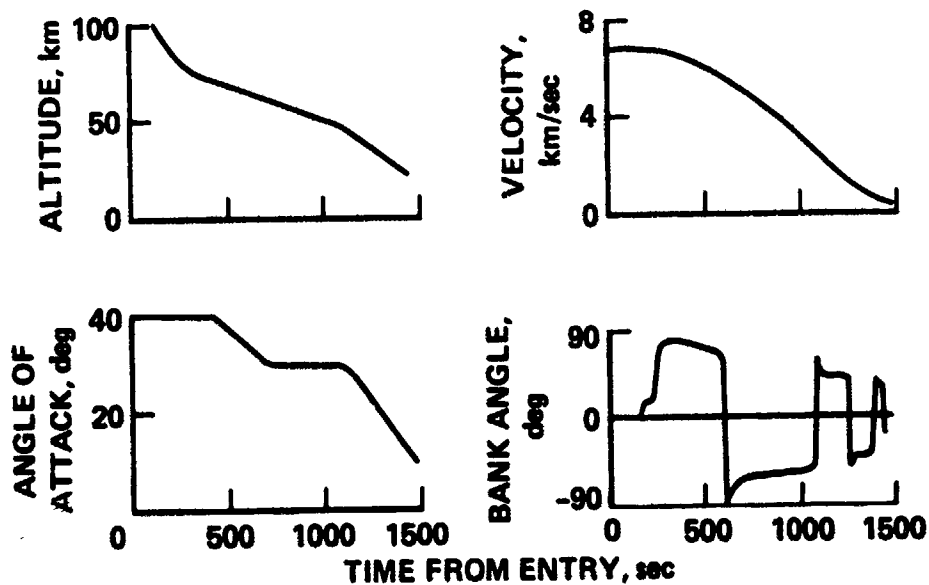


Figure 2.- Nominal entry trajectory characteristics.

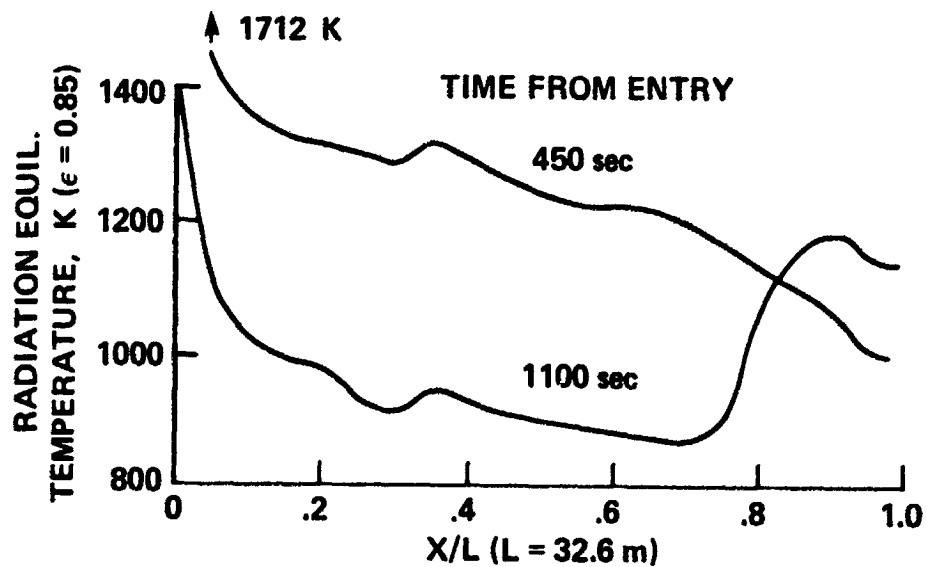


Figure 3.- Centerline temperature distributions.

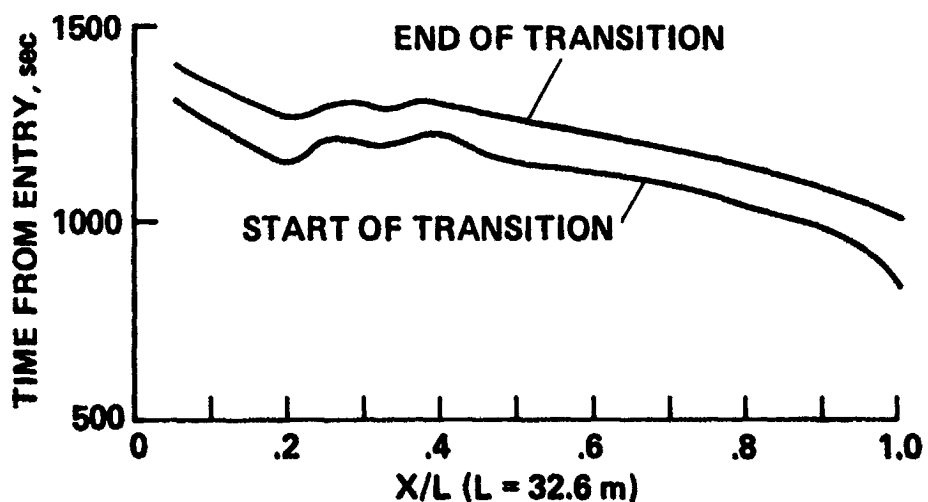


Figure 4.- Centerline transition location.

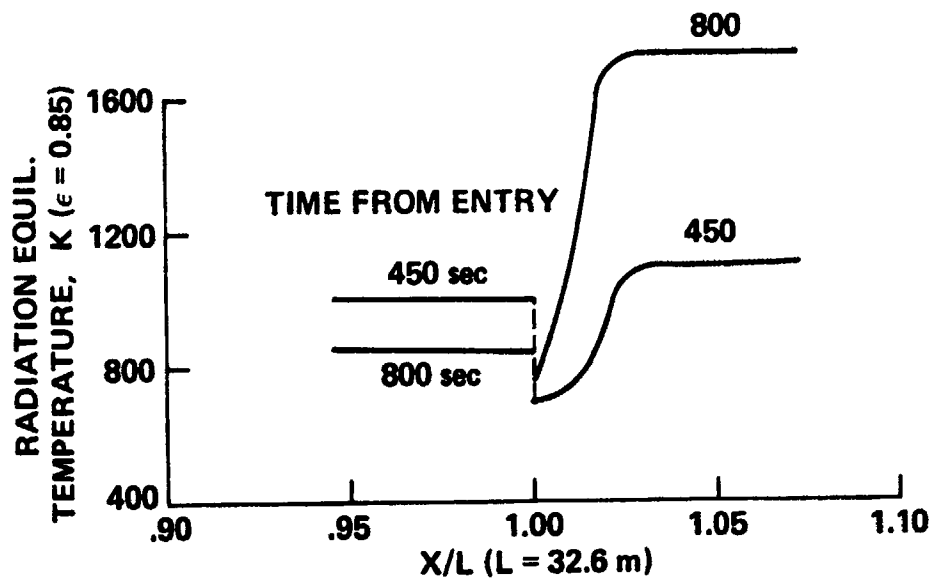


Fig 5.- Body-flap juncture temperature distributions.

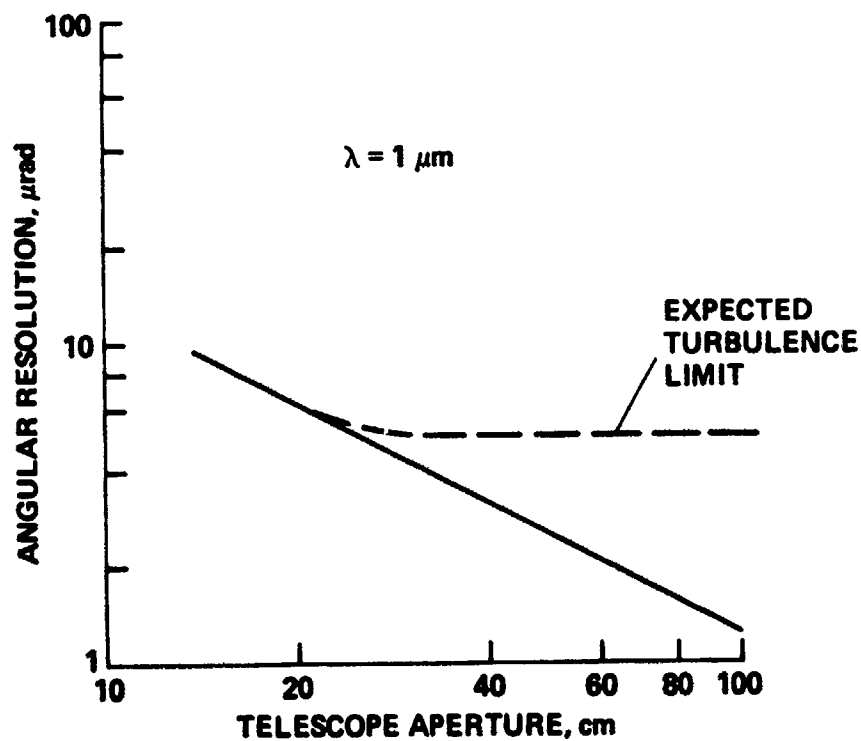


Figure 6.- Diffraction limited resolution performance.

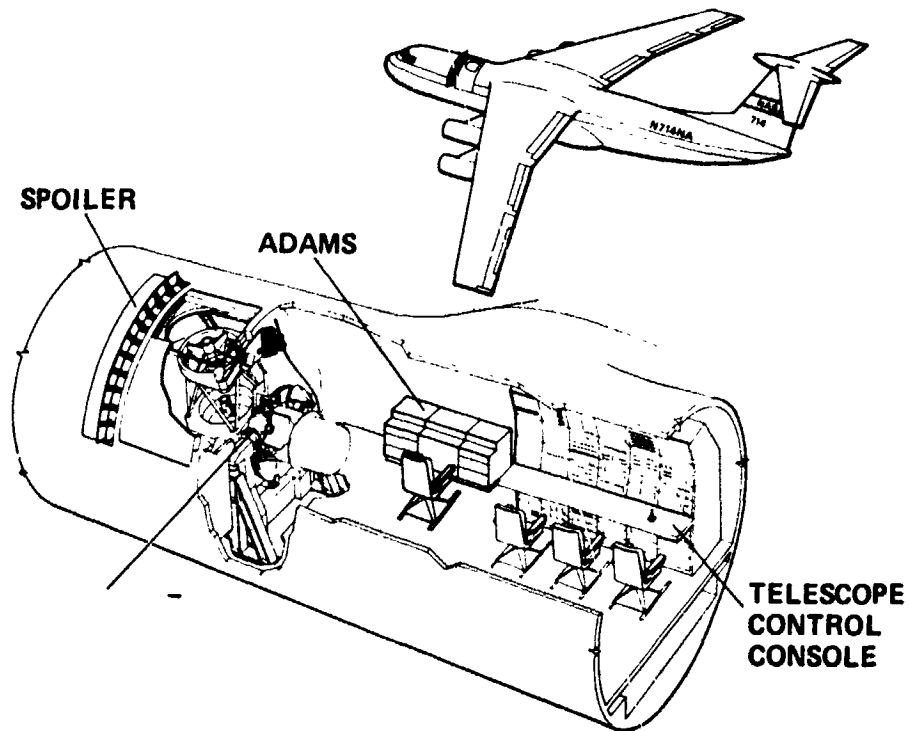


Figure 7.- C-141 airborne infrared observatory.

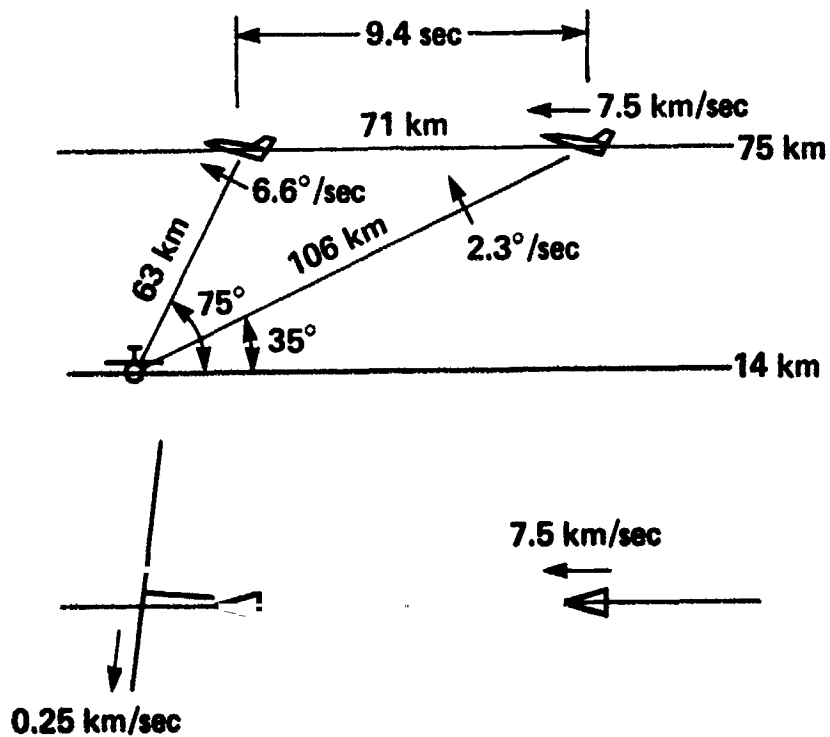


Figure 8.- Target acquisition mode geometry.

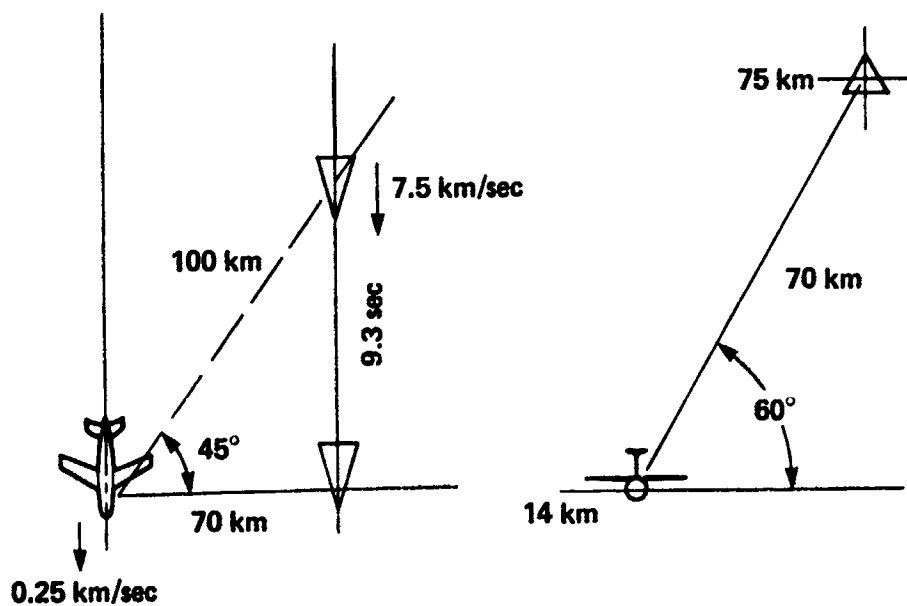


Figure 9.- Path acquisition mode geometry.

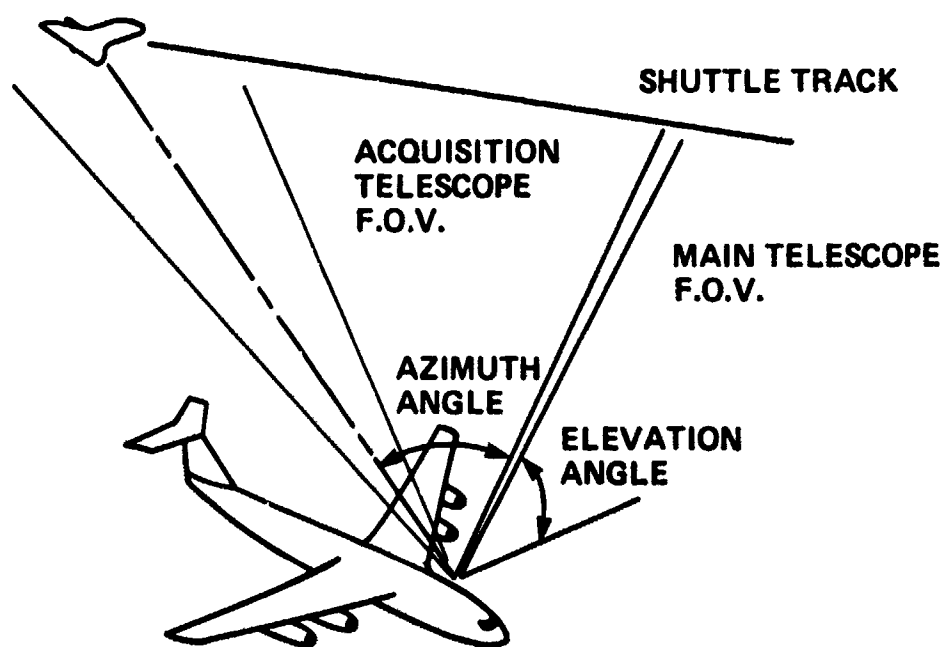


Figure 10.- Path acquisition schematic.

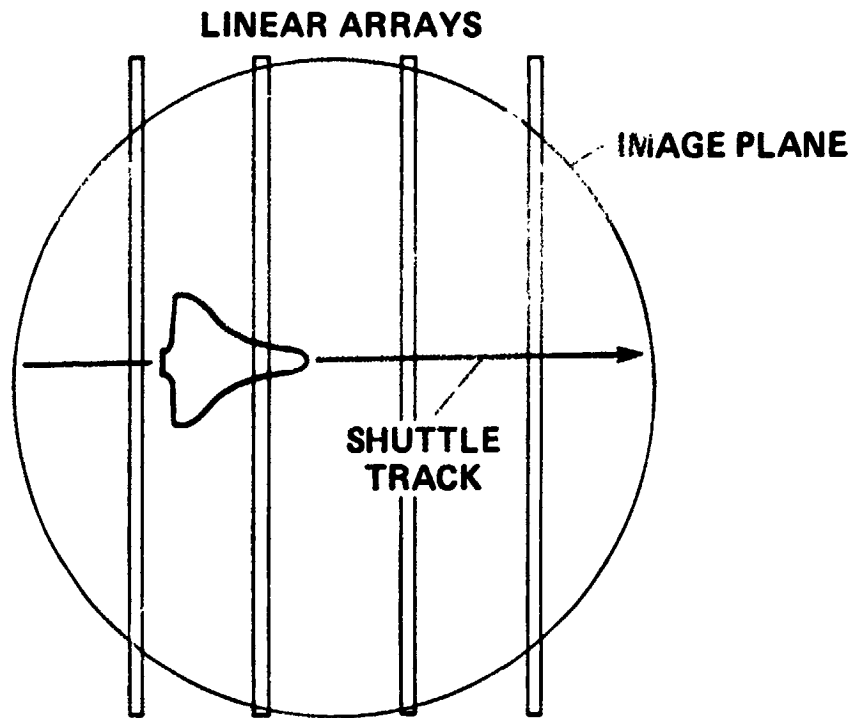


Figure 11.- Focal plane schematic.

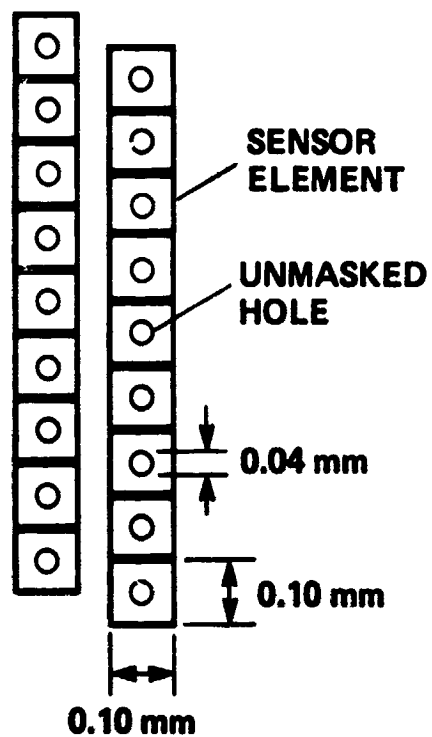


Figure 12.- Staggered linear array.

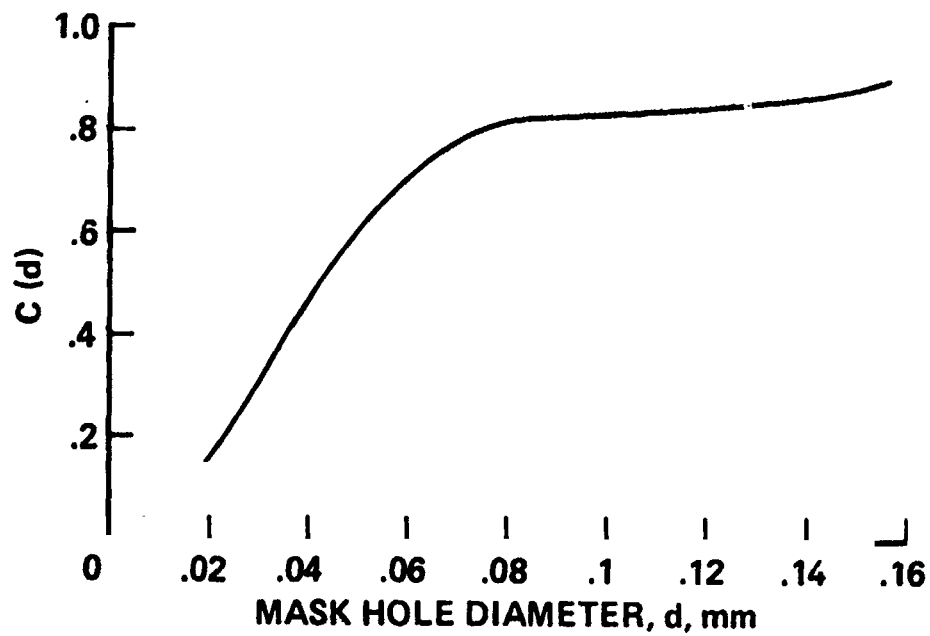


Figure 13.- Power fraction received by sensor element.

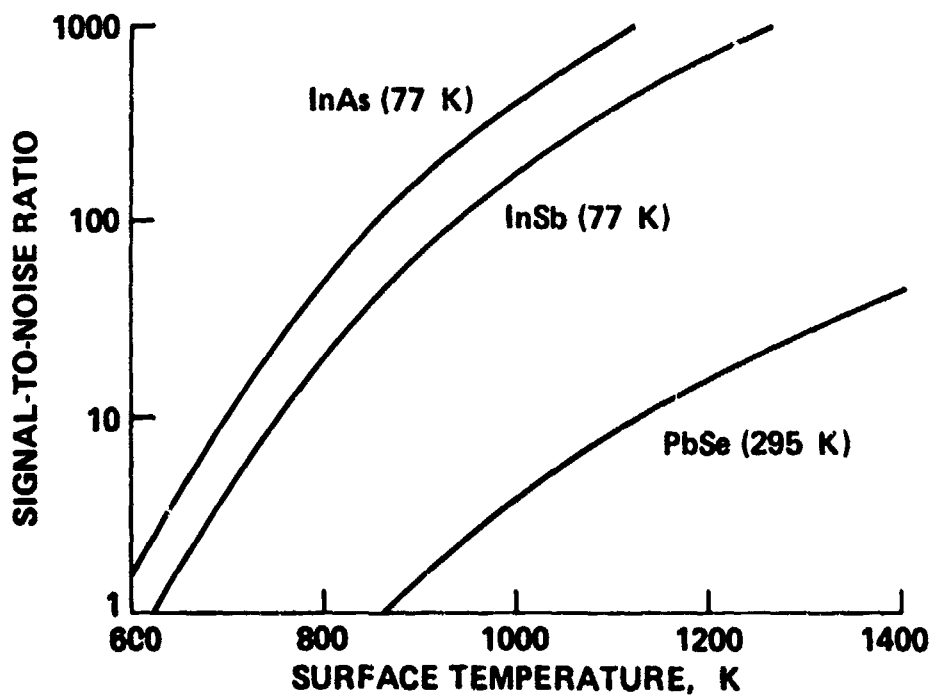


Figure 14.- Primary sensor performance.

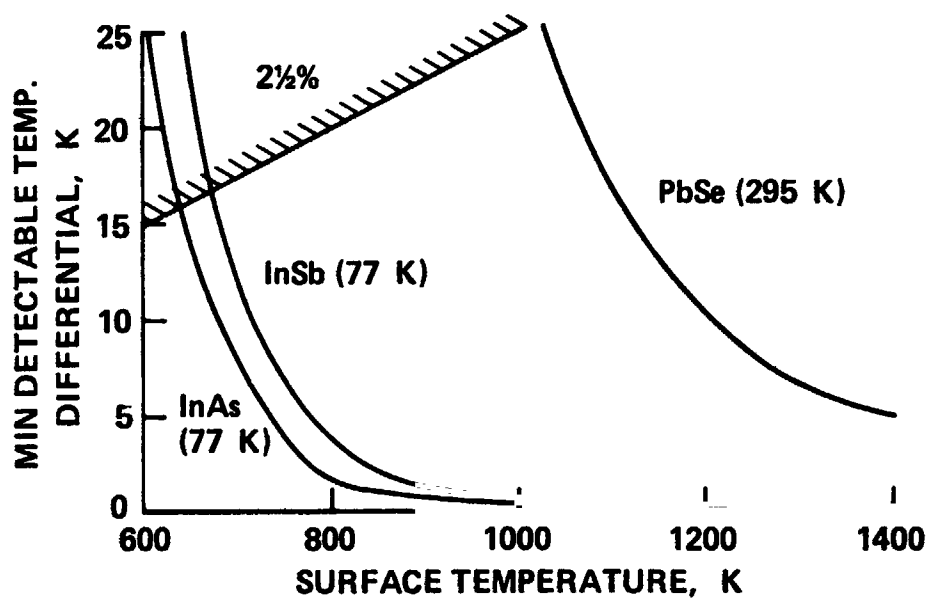


Figure 15.- Minimum temperature differential detectability.

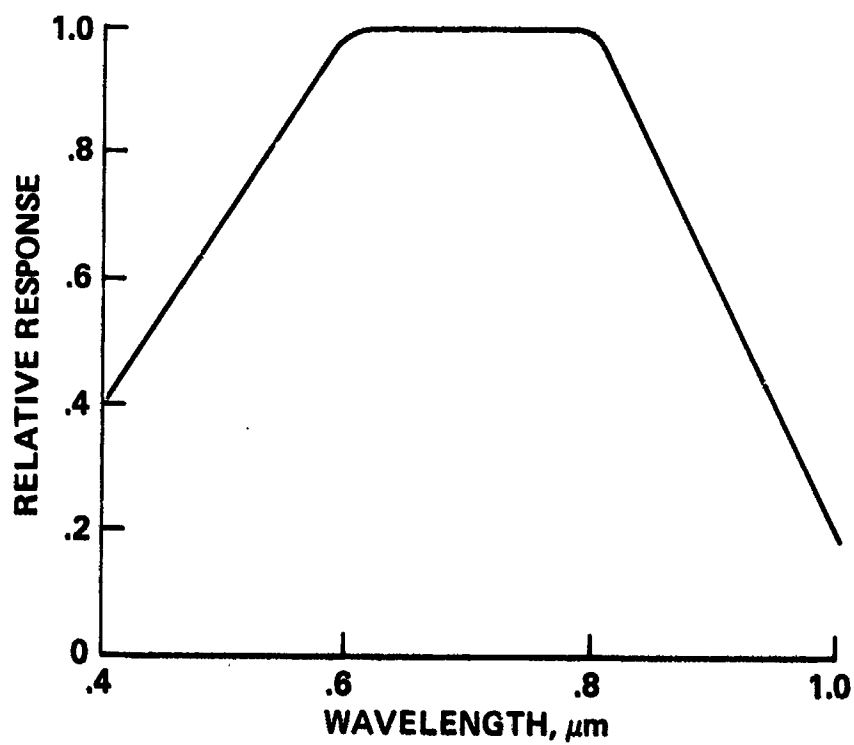


Figure 16.- Relative response of CCD arrays.

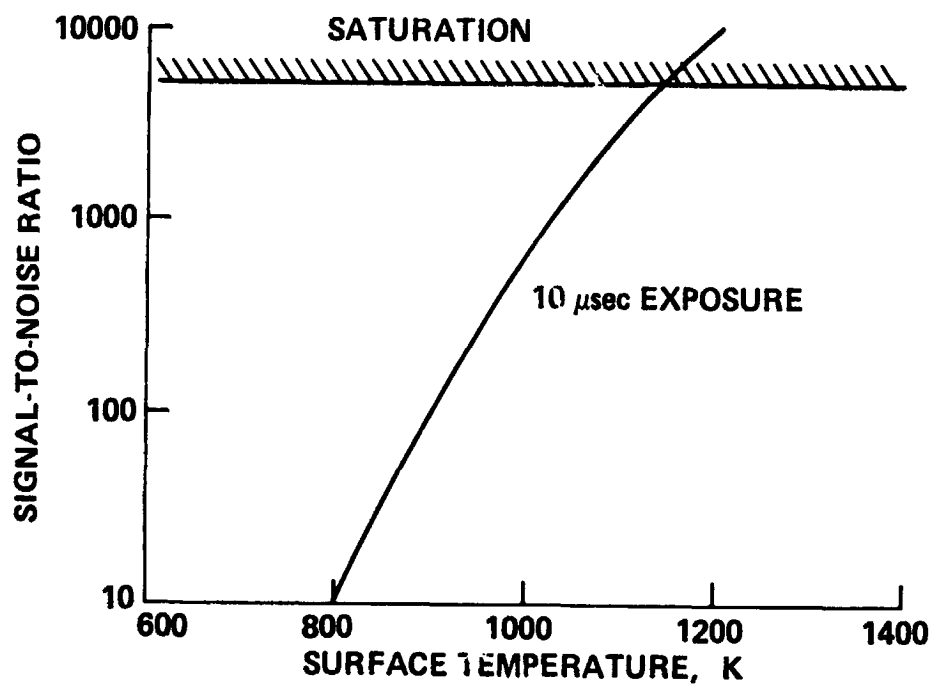


Figure 17.- CCD sensor performance.

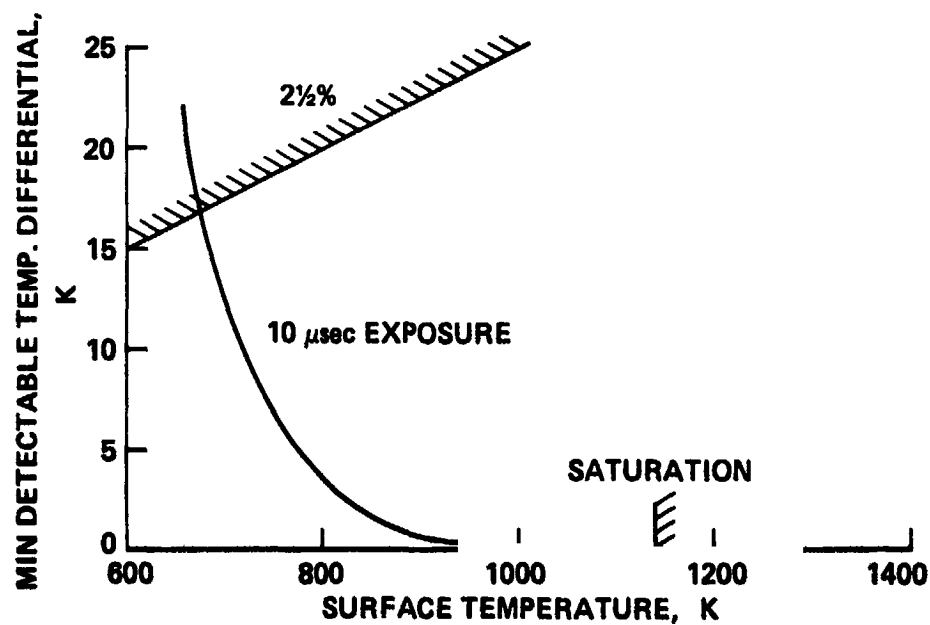


Figure 18.- Minimum temperature differential detectability for CCD arrays.

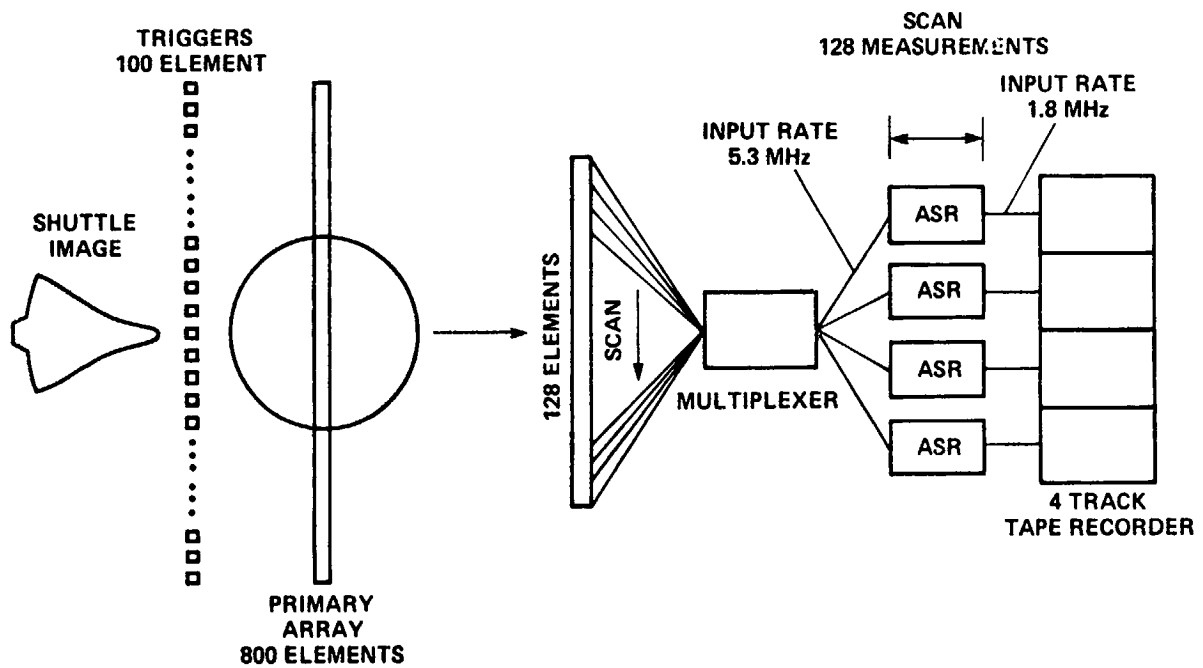


Figure 19.- Data handling system schematic.